PHOTOLUMINESCENCE OF INDIUM GALLIUM ARSENIDE QUANTUM DOTS AND DOT CHAINS

by

Aaron Mitchell Jones

A senior thesis submitted to the faculty of

Brigham Young University

in partial fulfillment of the requirements for the degree of

Bachelor of Science

Department of Physics and Astronomy

Brigham Young University

April 2010

BRIGHAM YOUNG UNIVERSITY

DEPARTMENT APPROVAL

of a senior thesis submitted by

Aaron Mitchell Jones

This thesis has been reviewed by the research advisor, research coordinator, and department chair and has been found to be satisfactory.

Date	John S. Colton, Advisor
Date	Eric Hintz, Research Coordinator
Date	Ross Spencer, Chair

ABSTRACT

PHOTOLUMINESCENCE OF INDIUM GALLIUM ARSENIDE QUANTUM DOTS AND DOT CHAINS

Aaron Mitchell Jones

Department of Physics and Astronomy

Bachelor of Science

Nanostructures such as quantum dots (QDs) and QD chains have received significant attention because of their applications in quantum information technologies. This paper presents optical investigations of InGaAs QDs and dot chains. The InGaAs samples were grown on a (001) GaAs substrate by Dr. Haeyeon Yang using a novel method similar to the Stranski-Krastonov growth method. Intensity and temperature dependence of the sample photoluminescence (PL) spectra were obtained through optical excitation and detection. The presence of a PL peak at $\sim$1 μm suggests the successful creation of QD chains. Also outlined is the method for calculating the PL curve-correcting functions to account for grating efficiencies and a changing reciprocal linear dispersion in monochromators.

ACKNOWLEDGMENTS

I would like to thank all who have spent their time reading and re-reading my thesis, helping shape it into what it is today. I would especially like to thank those in my research group for their ideas, help, and support with this research. Specifically, thanks to Dallas Smith, Scott Thalman, and Ken Clark for setting up the experiments and taking much of this data. My advisor, John Colton, deserves a special thank you for his advice, dedication to helping me succeed, and the countless hours spent teaching and re-teaching ideas connected with this research. His constant patience and teaching has helped me to learn much. I'd also like to thank my family for their enthusiasm and interest in my physics career. They have always encouraged me to give my best in everything I do. My greatest gratitude goes to my wife, Megan, for putting up with all the physics jokes, the late nights doing homework/research, and trying to act interested in my research. Her positive attitude and endless support is what keeps me going.

Contents

Table of Contents **vi**

List of Figures **viii**

1 Quantum Structures **1**
1.1 Characteristics of Quantum Dots 1
1.2 Creating Quantum Dots 2
1.3 Characteristics of Quantum Dot Chains 4
1.4 Creating Quantum Dot Chains 5

2 Experimental Method **8**
2.1 Schematic of PL Experiment 8
2.2 Sample Preparation 9
2.3 Data Collection Technique 10
2.3.1 Cryostat 10
2.3.2 Ti:Sapph Laser & Power Controller 10
2.3.3 Fiber Optic 10
2.3.4 Lenses and f-number Matching 11
2.3.5 Monochromator Gratings 12
2.3.6 Germanium Detector 12
2.3.7 Lockin Detection and Laser Chopper 13
2.4 Beam Width Measurement 13

3 Results and Discussion **15**
3.1 Possible Features 15
3.2 First Sample Class - With 1 μm Peak 16
3.2.1 Sample 032607A 17
3.2.2 Sample 032607B 18
3.2.3 Sample 032907 19
3.3 Second Sample Class - Without 1 μm Peak 20
3.3.1 Sample 022807 20
3.3.2 Sample 030607A 20
3.3.3 Sample 030607B 21

3.3.4 Sample 030907A 21
3.3.5 Sample 030907B 21
3.3.6 Sample 040307 22
3.3.7 Sample 040607 22
3.3.8 Sample 041007A 22
3.3.9 Sample 041007B 22
3.3.10 Sample 041707A-GC1 23
3.3.11 Sample 041707A-GC2 23
3.3.12 Sample 041707B 24
3.3.13 Sample 042207A 24
3.4 Future Studies 24

4 Conclusion **30**

A Table of Growth Parameters **31**

B Grating/Detector Response Correction **33**
B.1 DK 240 Monochromator Gratings 33

C Reciprocal Linear Dispersion Calculation **35**

Bibliography **37**

List of Figures

1.1 2D-3D Morphology Transition 5
1.2 Conventional and Novel Growth Method 6
1.3 Quantum Dashes and Quantum Dot Chains 6
1.4 Chevrons from RHEED Imaging 7

2.1 Schematic of Experimental Setup 9
2.2 Diagram of f-number Matching 11

3.1 State-Filling Effect 16
3.2 Two Samples with Sharp 1 μm Peak 18
3.3 One Sample with Sharp 1 μm Peak 19
3.4 Samples without Sharp 1 μm Peak 25
3.5 Samples without Sharp 1 μm Peak 26
3.6 Samples without Sharp 1 μm Peak 27
3.7 Samples without Sharp 1 μm Peak 28
3.8 Samples without Sharp 1 μm Peak 29

B.1 Grating Response Curves 34

C.1 Diagram of Czerny-Turner Monochromator 36
C.2 Data Corrected for Changing Reciprocal Dispersion 37

Chapter 1

Quantum Structures

1.1 Characteristics of Quantum Dots

Creating nanostructures in which quantum effects are dominant has become the subject of much research since such structures exhibit quantum-mechanical properties such as discrete electron energy states. These well-defined energy levels result in discrete emission and excitation energies with certain allowed and forbidden transitions between states. Quantum dots (QDs) are zero-dimensional nanostructures created by confining a small number of electrons in all directions. The confinement occurs by creating a potential barrier around the electrons. Nanostructures with less confinement include quantum wires (QWrs) and quantum wells (QWs). QWrs are one dimensional structures, limited in size in the other two dimensions. QWs are two dimensional structures, confined in only one dimension.

One system that exploits electron energy quantization is the quantum dot infrared photodetector (QDIP). Liu *et al.* has created QDIPs with greater efficiency than quantum well infrared photodetectors [1]. These detectors clearly exhibit energy quantification and show effects of state-filling in the s, p, d and f orbitals. The state-

filling occurs when a high excitation intensity pumps electrons into a state more quickly than the electrons can transition to a lower state. By simply altering the quantum dot size and concentration, custom detectors can be created. Other systems which use quantized energy levels include proposed quantum computation schemes and LEDs.

Another motivation for the development of QDs is the creation of 1.3 μm lasers for use in short-range optical communications systems [2]. The size of the QD determines the energy levels and hence the emission wavelengths. Since QD size can be controlled during the growth process, lasers of virtually any wavelength (including 1.3 μm) can be created [3–5].

1.2 Creating Quantum Dots

Common materials for creating QDs include gallium arsenide (GaAs), indium arsenide (InAs), indium gallium arsenide (InGaAs), silicon, germanium, and cadmium selenide (CdSe). Four typical methods of QD formation are: (1) creating dots through QW interface fluctuations, (2) lithographically defining QDs, (3) growing self-assembled quantum dots (SAQDs) and (4) creating nanocrystals in solution ("colloidal QDs").

The first three of these methods use molecular beam epitaxy (MBE) for QD formation. The MBE growth method heats up an element in a vacuum, allowing atoms to "burn off." This creates a beam of atoms directed toward the sample substrate. The desired concentration of atoms in the sample is attained by controlling (via temperature) the relative strength of the different beams. Since multiple beams can be accurately directed at the sample in exact proportions, MBE is often the preferred method of growth for high quality, low impurity research samples. However, the increased control in MBE comes at a cost of long growth times, rendering the method

impractical for industrial applications.

Quantum dots formed through interface fluctuations are created by interrupting the MBE growth of narrow QWs. This causes the QW width to fluctuate by one atomic layer ("monolayer"). The QDs form in the QW at locations where the material interface (i.e. between AlGaAs and GaAs) accumulates an extra monolayer [6]. The additional monolayer provides a lower potential region than in the surrounding area, forming a localized QD. However, the formation of these dots is random and therefore unsuitable for applications requiring a high degree of controllability.

Lithographically-defined quantum dots (LDQDs) are created by confining electrons with a voltage applied to metallic leads. A heavily doped, QW-like layer is grown on the substrate, after which the layer is capped with the same material as the substrate. The leads are then created on top of the capping layer through photolithography and chemical etching. A negative voltage applied to the leads electrostatically repels the electrons in the QW below, creating an insulating potential barrier for the inner electrons and forming a localized QD. One disadvantage of LDQDs stems from their method of creation. Even when using electron beam lithography, the linear dimension of the QD is usually greater than 10nm, offering less confinement than other growth methods [7].

Self-assembled quantum dots (SAQDs) form during MBE growth when the difference in lattice parameters (between 2% and 10%) creates strain. This strain in the wetting layer, or initial growth layers, grows as more monolayers accumulate until it is energetically favorable to form three-dimensional islands on the wetting layer surface. Three-dimensional islands then form due to the lattice "buckling." This method of forming SAQDs in III-V semiconductors is known as the Stranski-Krastanov growth method. These dots are often only a few nanometers high and approximately 20 nm wide for InGaAs dots grown on GaAs [8]. For a thorough discussion of SAQDs, see

references [7] and [9].

Semiconductor nanocrystals, also known as colloidal QDs, are chemically created and suspended in aqueous or organic solutions. The nanocrystal size sensitively depends on the formation temperature and solution concentrations and often only measures a few nanometers in each direction. For more information regarding semiconductor nanocrystals, see references [7] and [10].

1.3 Characteristics of Quantum Dot Chains

A QD chain consists of a row of QDs where inter-dot spacing is small enough to allow interactions between the wave functions of neighboring dots. QD chains have applications in quantum computing schemes where spin information can be transmitted through Rabi waves over short distances through the chain [11, 12]. Since the spin-state information can be transferred without modulating any fields, these chains could connect different elements of a quantum computer and perhaps even connect them to conventional silicon-based computers [11].

QD lasers have received considerable attention due to their emission in the 1.3 μm regime which is particularly useful for fiber optic communication [13]. The creation of QD chains consisting of evenly-spaced QDs could allow for the development of lasers of arbitrary wavelengths [14]. Since the interactions between QDs depend on their spacing, altering the spacing in QD chains would change the energy levels and hence emission wavelengths. If arrays of QD chains consisting of evenly-spaced QDs can be created with a high degree of homogeneity, they could serve as narrowband infrared lasers of arbitrary wavelength. Additionally, the wavelength could be further modified by varying the QD composition within the chain.

1.4 Creating Quantum Dot Chains

The conventional, or Stranski-Krastonov, growth method for SAQDs is comprised of three steps. First, the oxide layer, which comes with a purchased sample, is desorbed in vacuum at 620°C. Second, a smooth substrate forms by growing a GaAs buffer layer at 580°C. Lastly, the wetting layer grows thicker and thicker until the formation of 3D surface islands is energetically more favorable than continued layer-by-layer growth. This happens once the elastic strain energy exceeds the energy barrier to 3D formation as shown in Fig. 1.1 and causes the lattice to buckle [15]. The wetting layer thickness at which SAQDs form ("critical thickness") for InGaAs on GaAs is ∼6 monolayers (MLs) with the conventional growth method (CGM).

Dr. Haeyeon Yang of Utah State University has developed a new method to more accurately control the creation of InGaAs QDs [16]. His method uses MBE growth at a lower temperature to create a wetting layer above the critical thickness for three-dimensional structure formation to occur. This allows the size and spacing of the InGaAs nanostructures to be controlled by altering the thickness of the InGaAs wetting layer [5, 16]. The formation of QD chains in InGaAs on GaAs occurs once the wetting layer reaches a thickness of ≈10.7 MLs. This thicker wetting layer also suppresses indium segregation and intermixing, creating more homogeneous QDs.

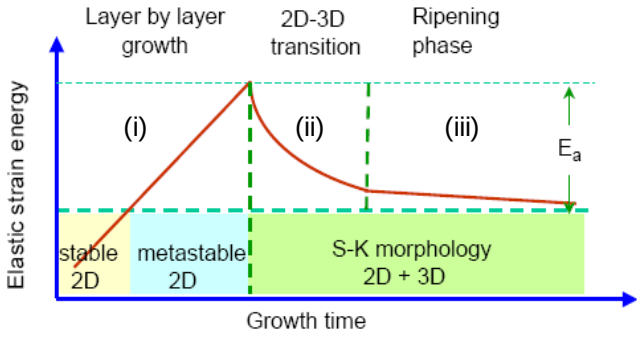

Figure 1.1 A strain-induced 2D to 3D transition occurs when the elastic strain energy on the surface exceeds the energy barrier for 3D formation, E_a (from reference [15]).

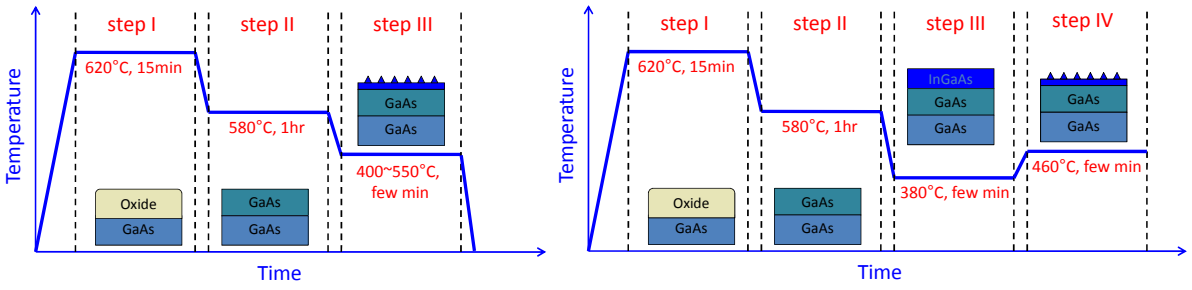

(a) (b)

Figure 1.2 The conventional Stranski-Krastonov growth method is shown in part (a). Yang's new growth method, shown in (b), differs from the CGM in the third step. The InGaAs wetting layer is grown at a lower-than-normal temperature and then annealed at a higher temperature (from reference [5]).

Creating a thicker wetting layer (and forming QD chains) requires dividing in two the final step of the CGM (compare step III in Fig. 1.2(a) with steps III and IV in Fig. 1.2(b)). First, the InGaAs wetting layer is grown at a lower temperature than in the CGM. The lower temperature increases the energy barrier to 3D island formation, allowing the wetting layer to grow thicker before forming QDs. Next, sample annealing at a higher temperature provides greater atomic mobility, and allows QDs, dashes (Fig. 1.3(a)) or QD chains (Fig. 1.3(b)) to form. The growth process is monitored *in situ* using reflection high energy electron diffraction (RHEED) in which electrons scatter off of the sample and create a diffraction pattern. The appearance of chevrons in the diffraction pattern indicates the successful creation of QDs (see

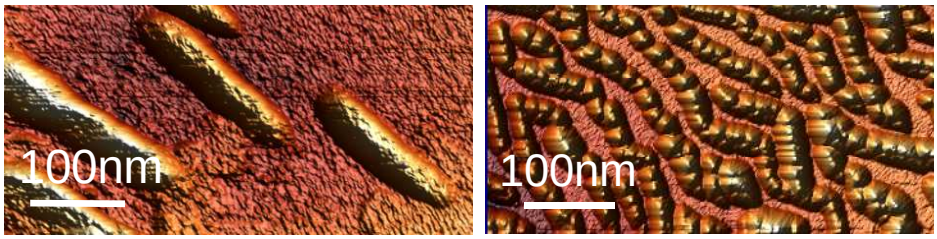

(a) (b)

Figure 1.3 By varying the thickness of the wetting layer, Yang's new growth method can produce (a) quantum dashes and (b) QD chains (rows of QDs). Images from reference [5].

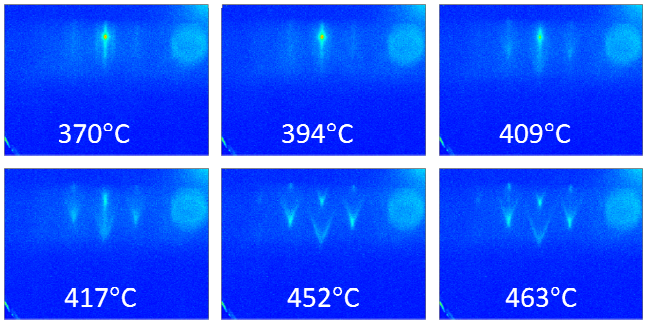

Figure 1.4 RHEED chevrons appear as the annealing temperature is increased, indicating the formation of QDs (from reference [17]).

Fig. 1.4).

The formation of InGaAs QD chains on GaAs substrates has previously been accomplished by Z.M. Wang [3, 4, 18]. However, Wang's most recent QD chains were grown on a pre-patterned GaAs substrate using the CGM, whereas Yang used an unpatterned substrate with his growth method. As of 2008, the growth of InGaAs quantum dashes and QD chains on (001) GaAs using this new method had only been accomplished by Yang [5].

Chapter 2

Experimental Method

2.1 Schematic of PL Experiment

Due to the emission of discrete energies (and hence wavelengths) from QDs and QD chains, perhaps the most straight-forward method of sample characterization is photoluminescence (PL) spectroscopy [19]. We studied the samples grown by Dr. Haeyeon Yang using PL spectroscopy to probe their energy level configuration.

In PL spectroscopy of a semiconductor, the material is optically excited by a laser with a wavelength short enough (high enough energy) to cause an electron to transition from the valence band to the conduction band. In the case of QDs, the laser energy causes transitions between quantized energy levels. As the electron relaxes back to the lower energy state, it emits a photon with an energy equal to the conduction band and valence band separation ("band gap"). The total emitted PL resulting from the transitions of many electrons can be spectrally analyzed by a monochromator and detector. The spectral distribution of the PL is determined by plotting the light intensity at the detector versus the wavelength exiting the monochromator. Fig. 2.1 shows the experimental setup for the InGaAs QD chain PL experiments.

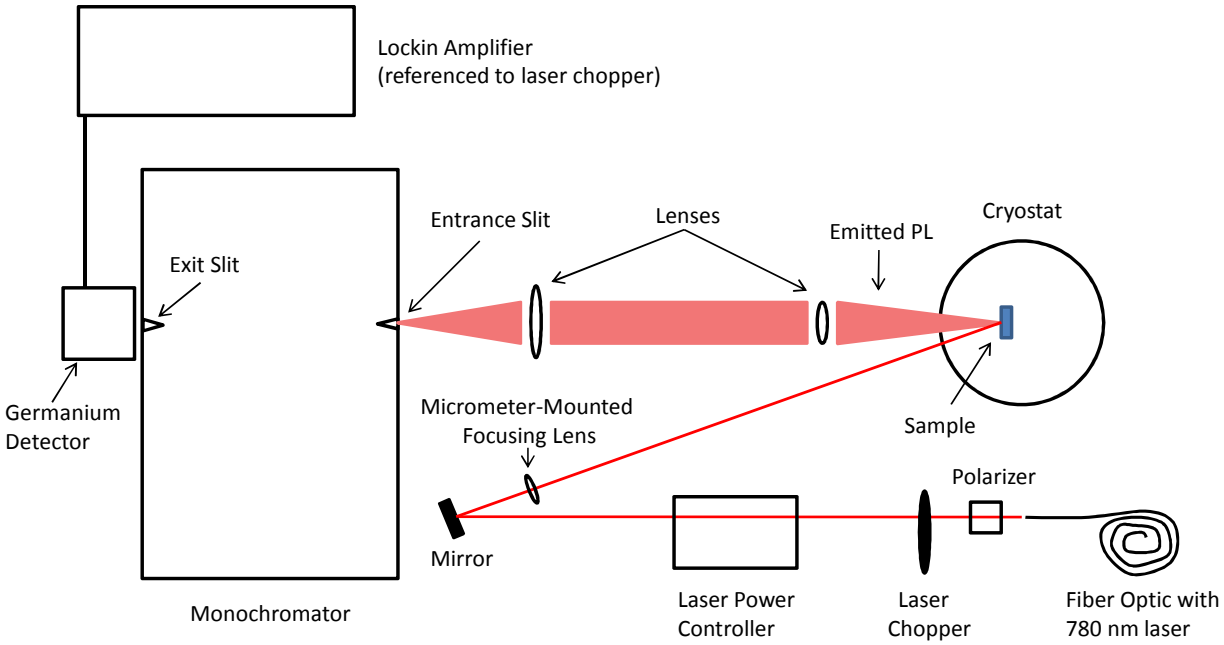

Figure 2.1 InGaAs PL experimental setup.

2.2 Sample Preparation

Samples grown through MBE tend to have more homogeneous concentrations in the center of the sample where the molecular beams are more uniform and well-defined. Dr. Yang coated the outer edge of each sample with an indium seal which, after cleaving the initial sample into four squares, served to indicate the two outer edges on each. The best part of the sample with the highest degree of homogeneity (the "good corner") could then be identified as being opposite these two edges. We were sent only one of the four squares for each sample. We then cleaved each of these squares into smaller segments in order to fit as many samples as possible inside the cryostat's small probe window. After our cleaving, each good corner measured approximately 2 mm by 2 mm. Refer to Table A.1 in Appendix A (page 32) for specific growth parameters for each sample.

2.3 Data Collection Technique

2.3.1 Cryostat

The samples were stuck to the cold-finger of a CryoIndustries 1.5 W cryostat using vacuum grease. The cryostat's normal temperature range of 4 - 50 K was extended to 300 K for temperature dependence studies by connecting an additional power supply to a secondary resistor heater.

2.3.2 Ti:Sapph Laser & Power Controller

The samples were optically excited at near-normal incidence with an adjustable-wavelength Spectra Physics 3900S Ti:Sapph laser pumped by a Spectra Physics Millennia V laser. The wavelength was chosen so that the photon energy lay above the GaAs band gap, corresponding to a wavelength choice of 780 nm [20]. To probe a small subset of QDs, the laser was tightly focused (within the Rayleigh range) onto the sample. To ensure a constant intensity at the sample area, a BEOC power controller stabilized the laser power to within 0.1%.

2.3.3 Fiber Optic

A fiber optic cable carried the laser beam from one optical table to the other. This avoiding shining a powerful beam across the open space between optical tables. The fiber used was an Oz Optics LPSC-04 adjustable focus single-mode fiber. Although not a polarization maintaining fiber, laser polarization often exceeded 90%. The polarization direction stability, however, depended sensitively on the physical positioning of the fiber. Extra care was taken not to bump the fiber since a small change in polarization could significantly affect the performance of the power stabilizer and

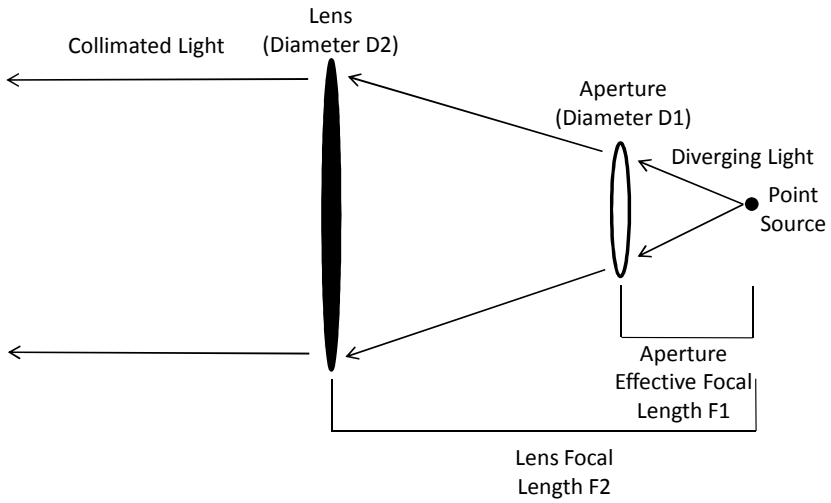

Figure 2.2 Diagram of f-number matching.

perhaps affect the laser intensity.

2.3.4 Lenses and f-number Matching

To collimate the sample PL, a lens's f-number must match the f-number of the cryostat's optical access[1] (see Fig. 2.1). The f-number of a lens or piece of equipment is given by

$$\text{f-number} = f/D, \tag{2.1}$$

where f is the focal length and D is the effective aperture diameter (see Fig. 2.2). The focal length of the lens nearest the cryostat was chosen to be long enough so that the laser beam incident on the sample did not enter the lens. The collimated PL then passed through a lens f-number-matched to the monochromator. Matching the f-number maximizes spectral resolution within the monochromator since an f-number-matched beam illuminates the entire grating area.

[1]The cryostat's optical access was large enough that it did not significantly constrict the emitted PL. The PL was then collimated by simply placing the sample at the focal point of the lens.

To test the optical alignment, we illuminated the sample area at near-normal incidence with a flashlight. By placing a piece of paper over the entrance slit of the monochromator, the sample image could easily be seen at the monochromator. We then adjusted the lenses until the sharpest image formed at the monochromator. After the initial alignment, the collimating lens (nearest the samples) was no longer adjusted. Moving the focusing lens (nearest the monochromator) in the direction perpendicular to the beam could then align the current sample on the entrance slit of the monochromator since the samples were typically placed in a horizontal row.

2.3.5 Monochromator Gratings

The PL graphs were created by recording the light intensity at the Ge detector as a function of the wavelength exiting the CVI DK 240 monochromator. However, since all optical gratings have an inherent response curve, we calculated a correcting function to correct the data (see Appendix B). Also, due to a (nonlinearly) changing reciprocal linear dispersion, the range of wavelengths exiting the monochromator varied as a function of wavelength. Since this also affected the light intensity at the Ge detector, a wavelength dependent curve for correcting the PL data was also calculated. See Appendix C for this correction calculation and its effect on PL curves.

2.3.6 Germanium Detector

A liquid nitrogen-cooled EG&G Optoelectronics germanium detector detected the emitted PL. We sent the detector output to a lockin amplifier.

2.3.7 Lockin Detection and Laser Chopper

As shown in Fig. 2.1, the laser initially passed through a beam chopper. The chopping frequency of ∼320 Hz was chosen so as to not coincide with stray 60 Hz light sources in the lab. Background noise was reduced by referencing the lock-in to the beam chopper.

2.4 Beam Width Measurement

The beam area at the sample needed to be determined in order to report excitation intensities. To determine the beam width, we mounted a razor blade on a micrometer and, after moving the cryostat, placed it at the sample position. We then stepped the blade perpendicularly through the beam while monitoring the laser power on the far side of the blade. In order to avoid the effects of inconsistencies on the razor blade edge, we also measured the beam width with the blade turned at a sharp angle, making the blade nearly parallel to the beam. This effectively reduced edge roughness, theoretically allowing for a more accurate beam width measurement. We repeated this technique with a flat mirror turned at a sharp angle for comparison against the razor blade. However, both sharp-angle methods gave nearly the same beam width measurement.

We plotted the measured laser power versus micrometer position and then differentiated the curve to get the beam profile. A Gaussian fit of the beam profile then gave the beam width. The width reported by a Gaussian fit using MicroCal Origin - full width at ± one standard deviation - equals the half width at the $\frac{1}{e^2}$ peak power position. This is the effective beam radius. The intensity was then calculated[2] by

[2]The first experimental run used a Toptica DL 100 L laser at ∼820 nm which had an elliptical profile and some wavelength instability. These deficiencies were eliminated by switching to a cw

dividing the laser power by the excitation area:

$$Area = \pi * (width_{FW\sigma})^2 = \pi * (width_{\frac{1}{e^2}})^2. \tag{2.2}$$

Ti:Sapph laser. The beam of the first laser was elliptical in shape, requiring the beam width measurements to be performed in two directions. The two widths (averaged over many measurements) were $w_a = 0.1108\ mm$ and $w_b = 0.2479$ mm, giving a total area of 0.0137 mm^2 (using the equation of an ellipse - $Area = \pi * (w_a * w_b)/2$). All data presented in Figs. 3.2 - 3.3, however, used the Ti:Sapph laser.

Chapter 3

Results and Discussion

3.1 Possible Features

Common features of PL spectra for QDs include: the wetting layer (WL) peak, which occurs at a lower wavelength than QD emission; long-wavelength emission ($\sim 1.3\ \mu$m) often resulting from the emission of indium-rich regions; and, with high excitation energies, the state-filling effect.

The state-filling effect occurs when excitation energies are increased, filling the lower energy states of the QDs and causing excited states to radiate. As a result, the PL curve of QD samples often contains multiple, closely-spaced (or overlapping) peaks, as in figure 3.1 [19]. However, this effect was not observed in the samples we probed.

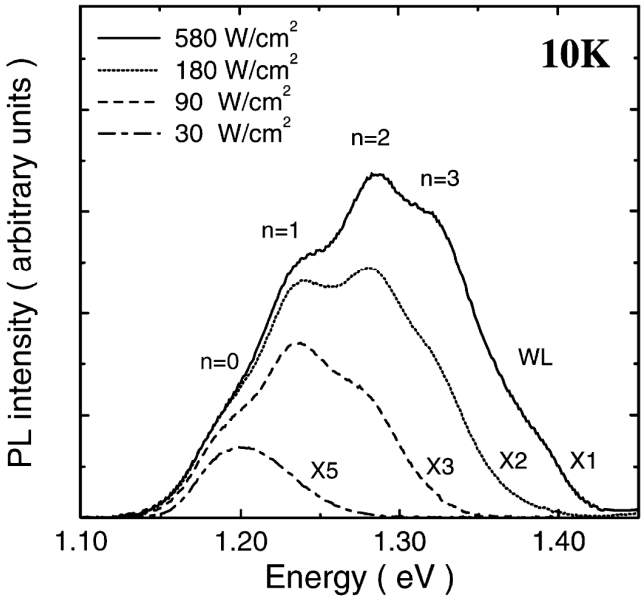

Figure 3.1 Multiple peaks resulting from state-filling in InGaAs QDs from W. Chang *et al.* (reference [19]).

3.2 First Sample Class - With 1 μm Peak

The photoluminescence curves shown in Figs. 3.2 and 3.3,[1] obtained using the cw Ti:Sapph laser, all exhibit a sharp peak just below 1 μm. This peak likely comes from QDs since the WL emits at lower wavelengths while indium-rich regions emit at longer wavelengths. Türck *et al.* found that emission from InGaAs QWs with widths varying from six to nine ML emitted at wavelengths of 924 nm to 971 nm, respectively [21]. After the initial growth, the InGaAs layer thickness in Yang's samples was 10 ML (for most samples). With annealing, the WL thickness decreases as the lattice buckles and forms 3D islands. The WL thickness for our samples would then be less than 10 MLs as atoms migrate from the growth layer to the energetically favorable 3D islands.

[1] All intensities given in Figs. 3.2 - 3.3 were obtained by calculating the beam radius at the $\frac{1}{e}$ intensity position. To obtain the intensity using the more conventional radius at $\frac{1}{e^2}$ intensity as discussed in section 2.4, divide all reported intensities by 2.

The lower-wavelength WL peak of ∼850 nm could stem from an indium-poor and/or thinner WL. Since indium leads to longer-wavelength emission, an indium-poor WL would naturally emit at lower wavelengths. A thin WL, perhaps only a few MLs thick, would exhibit greater electron confinement and produce higher energy (lower wavelength) emission. A combination of these two effects could produce the peak at ∼850 nm.

All of these samples also showed a broadband emission in the 1.3 μm range. This higher-wavelength peak stems from indium-rich regions. Although this wavelength is too low in energy to come from QDs, it may be of interest since it lies within the range for optical communication systems [13]. Increasing the sample temperature caused the 1 μm peak to shift to higher wavelengths (lower energy) due to a decrease in the band gap. Heating also likely explains the slight shift to higher wavelengths as power densities increase.

3.2.1 Sample 032607A

The "A" or "B" in the sample name indicates the first or second sample grown on that day, respectively. The WL growth for this sample lasted for 47 seconds with the arsenic valve at 25%, ending in a growth thickness of 10 MLs. The sample was then annealed at a temperature of 500 °C, but never produced chevrons in the RHEED pattern (see Fig. 1.4). The photoluminescence curves in Fig. 3.2(a) and Fig. 3.2(b) show a sharp peak at ∼950 nm for temperatures below 200 K. The disappearance of this peak at higher temperatures suggests the successful creation and probing of QD chains. In the power dependence study, the peak shift to longer wavelengths at 312 W/cm^2 likely stems from sample heating. This shift to longer-wavelength emission is also noticeable for higher temperatures in Fig. 3.2(b).

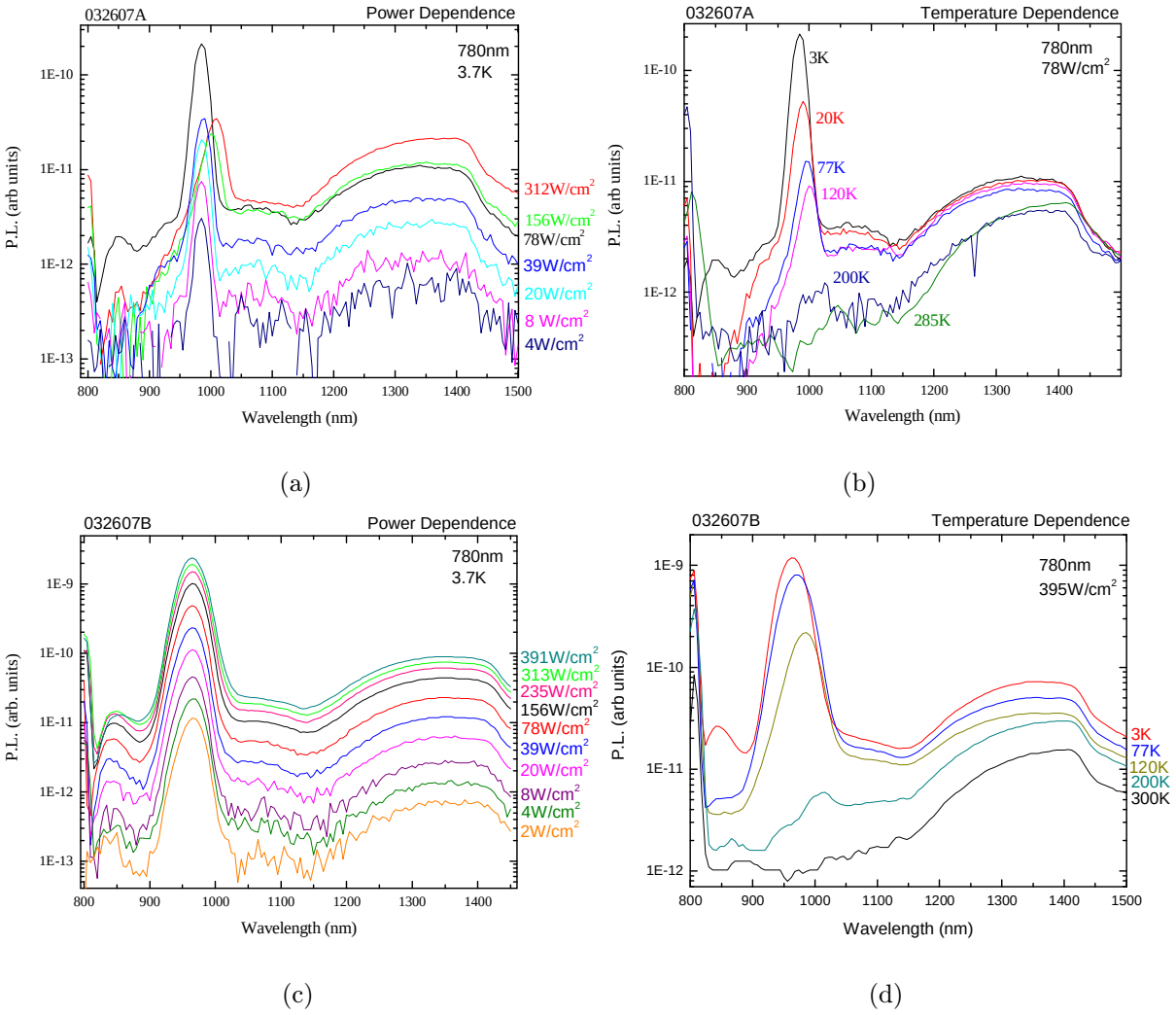

Figure 3.2 The sharp PL peak for the above samples may indicate the successful creation of QD chains. In all the temperature-dependence studies, 3K corresponds to 3.7K, the limit of our cryostat.

3.2.2 Sample 032607B

This sample was grown under similar conditions as sample 032607A, except the WL growth was performed with the arsenic valve at 40%, and was followed by a slightly higher annealing temperature of 540 °C. This sample did exhibit chevron patterns during RHEED. As with sample 032607A, there is a peak just below 1 μm, although broader in this case. Broader peak widths either indicate less homogeneous QD sizes

or perhaps provide more evidence of the creation of QD chains. The formation of QD chains causes a coupling between QDs, consequently changing the energy levels. A slightly irregular spacing between QDs in a chain would result in varying degrees of coupling and different energy levels in each dot, which could produce a broader PL peak as in Figs. 3.2(c) and 3.2(d).

3.2.3 Sample 032907

The growth of sample 032907 matches that of sample 032607A but with an annealing temperature of 520 °C. As with sample 032607A, no chevrons were apparent in the RHEED images. The PL spectra for this sample is shown in Fig. 3.3. Despite exhibiting a peak at near 1 μm similar to the previous two samples, its position does not change as excitation energy or temperature increases.

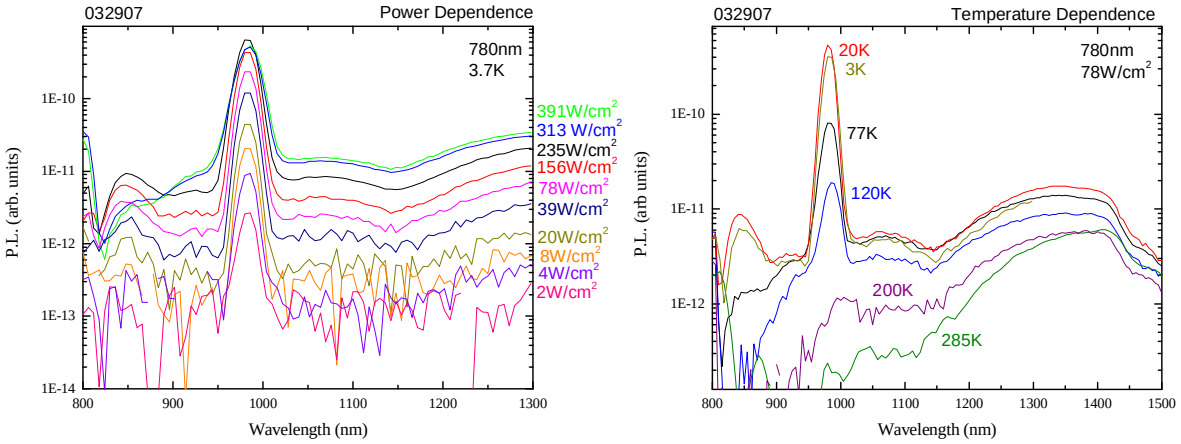

(a) (b)

Figure 3.3 The sharp PL peak in this sample may indicate the successful creation of QD chains.

3.3 Second Sample Class - Without 1 μm Peak

The photoluminescence curves shown in Figs. 3.4 – 3.7, obtained with the Toptica DL 100 L laser, do not exhibit the relatively sharp peak at ~ 1 μm. Many of these samples still showed the broadband emission in the 1.3 μm range as with the previous sample class. However, this broadband emission has a consistent downward slope in these samples, whereas the PL slopes upward from 1200 nm to 1300 nm with the previous samples. The downward sloping 1.1 μm - 1.4 μm emission for these samples likely results from indium-rich regions of varying concentrations in the WL. The cut-off near 1400 μm comes from our system's response.

3.3.1 Sample 022807

The annealing for this sample was at a lower temperature and for a longer duration than most of the other samples studied. Although not recorded, the growth thickness is likely greater than 10 MLs since the growth time is nearly double that for most other samples. This would result in a greater tension in the WL and the formation of larger QDs during annealing. Despite exhibiting chevron shapes during RHEED, the PL spectra for this sample did not exhibit the sharp 1 μm peak (see Figs. 3.4(a) – 3.4(b)). Instead, the sample showed broad emission at wavelengths over 1050 nm which could come from broad QDs covering nearly the entire sample surface.

3.3.2 Sample 030607A

The PL spectra of this sample show indications of a peak near 1.1 μm as in Figs. 3.4(c) – 3.4(d). As temperatures increased, the peak disappeared as with the previous sample class. The broader, longer-wavelength PL peak would suggest the formation of larger QDs or QD chains which do not exhibit high uniformity, since inhomogeneous

QD sizes lead to broadband emission. This can be explained by the the sample's thicker WL (1.5 times thicker than the previous sample class). A thicker WL creates more strain in the lattice, making it more energetically favorable to form surface islands. The longer annealing time and thicker WL could reasonably cause the initially small QDs to grow very large, and perhaps nearly cover the entire sample surface.

3.3.3 Sample 030607B

The growth of this sample matches that of sample 030607A from earlier the same day, but with the arsenic valve open to 12% during growth compared to 100% with the earlier sample. However, despite very different arsenic valve parameters, the PL spectra hardly differ as seen in Figs. 3.4(c) – 3.4(f). Thus, the percent opening of the arsenic valve did not significantly alter the growth of QDs for these conditions.

3.3.4 Sample 030907A

This sample was grown in the same manner as sample 032607A but with the arsenic valve reduced from 25% to 15%. Neither exhibited chevrons during RHEED. However, the lower arsenic percentage seems to have eliminated the formation of homogeneous QDs, perhaps leading to an over-crowding of 3D islands as evidenced by its broad, constant PL spectrum in Figs. 3.5(a) – 3.5(b).

3.3.5 Sample 030907B

The growth parameters for this sample are comparable to sample 030607B except for its thinner WL. The PL spectra are very similar (see Figs. 3.5(a) – 3.5(d)) and, despite this sample's smaller WL, large 3D island formation likely resulted.

3.3.6 Sample 040307

This sample was grown under similar conditions as samples 032607A and 032907, only changing the annealing temperature to 550 °C. Unlike those samples, though, chevrons did appear in the RHEED imaging. We looked at the position-dependence of the PL for this sample, but only found that heating caused the spectra to shift down over time while the overall shape remained constant. Increasing the excitation intensities in the power dependence study increased the overall background PL, but failed to produce a 1 μm peak.

3.3.7 Sample 040607

Few features beside the WL peak are evident in this sample's PL (see Figs. 3.6(a) – 3.6(b)). This may be a result of the thinner WL, 7.6 MLs. A thinner WL would introduce less strain compared to the other samples. If the strain is small enough that the energy barrier to 3D island formation is not overcome, then QD formation will not occur. Without the formation of QDs, the sample would be similar to a QW and perhaps emit like a WL.

3.3.8 Sample 041007A

We decided not to obtain any temperature dependent PL for this sample because of the virtually nonexistent PL in the power dependence study (compare P.L. intensity scales in Fig. 3.6(c) with surrounding figures).

3.3.9 Sample 041007B

The growth parameters for this sample were similar to those of sample 040607, but with a lower annealing temperature. The PL from both samples are nearly identical,

where both exhibit a WL-like peak near 900 nm (see Figs. 3.6(c) – 3.6(e)). However, the temperature dependent PL from sample 041007B does show a larger peak near 1080 nm, perhaps from large QDs.

3.3.10 Sample 041707A-GC1

GC1 in the sample name indicates that there was some ambiguity in determining which sample corner was closer to the center of the initial, larger sample. Thus, there are two sub-samples, each taken from a different, possibly good corner of the sample: 041707-A-GC1 and 041707-A-GC2. The sample annealing was performed at the lowest temperature of all samples. The WL thickness was 10 MLs as with the previous sample class. As shown in Figs. 3.7(a) – 3.7(b), the PL spectra exhibit a narrow-looking peak above 1 μm. As excitation intensities increased, the peak broadened, reminiscent of the state-filling effect. However, the state-filling effect leads to higher energy (lower wavelength) excitations, the opposite of what the spectra show. Significant sample heating could cause the broadened peak to shift to longer wavelengths, counteracting the lower-wavelength shift from state-filling.

3.3.11 Sample 041707A-GC2

This sample is just the other corner of the above sample. The temperature dependent PL spectra are similiar and initially the power dependence curves look the same. However, at higher powers, the sample's PL broadens more than with the previous sample (compare Figs. 3.7(a) – 3.7(d)). Again, this may stem from the combined effect of state-filling and heating.

3.3.12 Sample 041707B

This sample was prepared in the same manner as sample 041007B with a nearly identical PL spectrum (compare Figs. 3.6(d) – 3.6(e) and Figs. 3.7(e) – 3.7(f)).

3.3.13 Sample 042207A

This sample was prepared as with samples 041007B and 041707B, but annealed at a slightly higher temperature. It produced a broad PL peak near 1040 nm, especially at higher powers (see Figs. 3.8(a) – 3.8(b)), which may result from state-filling. The temperature dependence study shows the peak shifting to lower wavelengths (higher energies) as the temperature increases, indicative of the heating effects discussed earlier. Whether the higher-wavelength peak comes from larger QDs or QD chains cannot be determined, especially since the presence of chevrons during RHEED for this sample was not recorded. However, it is the peak at 980 nm (not seen here) that is most likely tied to QD chain formation.

3.4 Future Studies

Future experiments are planned to probe these samples with higher excitation energies. The samples will be placed in a liquid nitrogen immersion cryostat to better prevent sample heating. Once the excitation energies exceed $\sim$1 kW/cm^2, it is anticipated that we will observe the state-filling effect as in reference [19]. We also plan to probe the QD chains with a time-resolved method to determine the photoluminescence lifetime. This will allow for a more complete characterization of the QD chain samples since the PL recombination time will help determine which transitions are being excited.

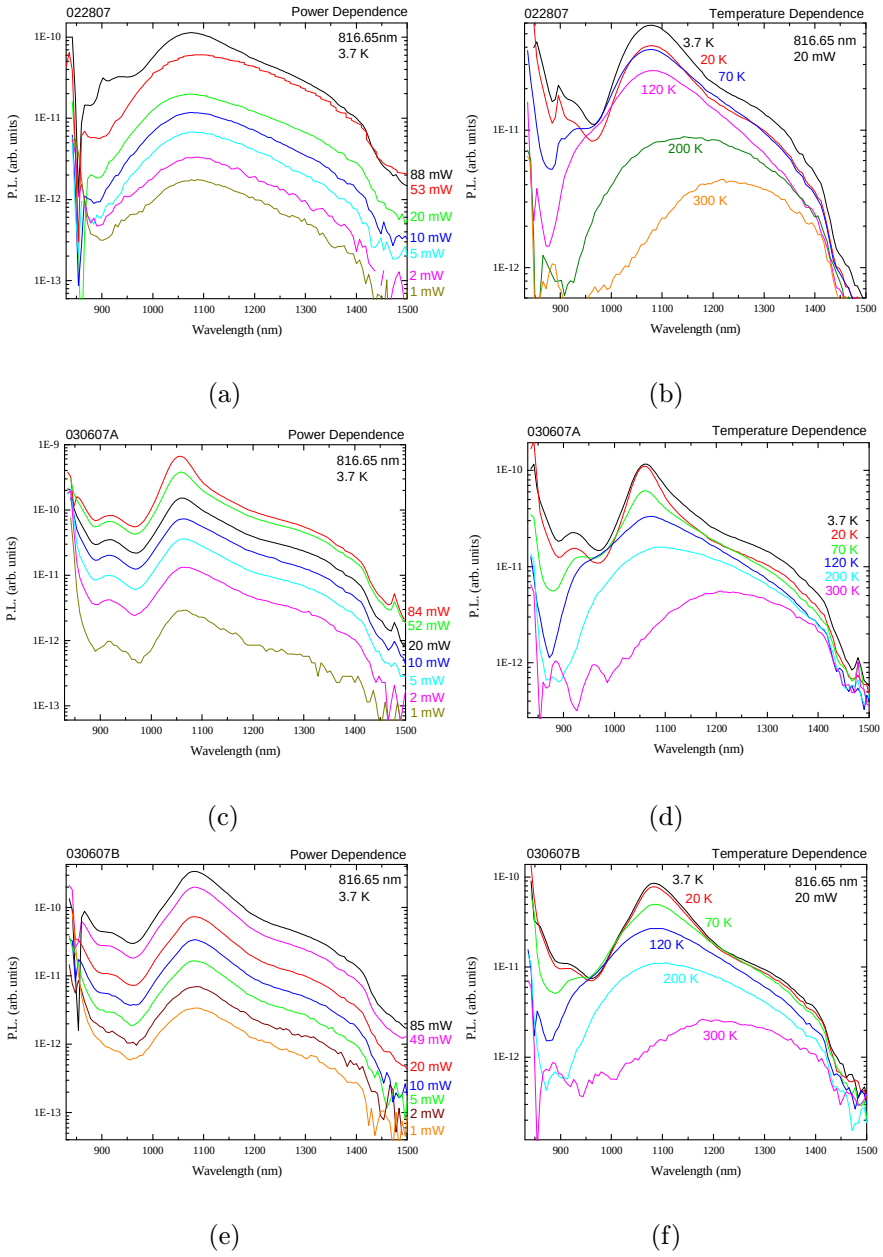

Figure 3.4 PL of samples 022807, 030607A, and 030607B. The peak below 1 μm, indicative of successful QD chain growth, is not present in these PL spectra.

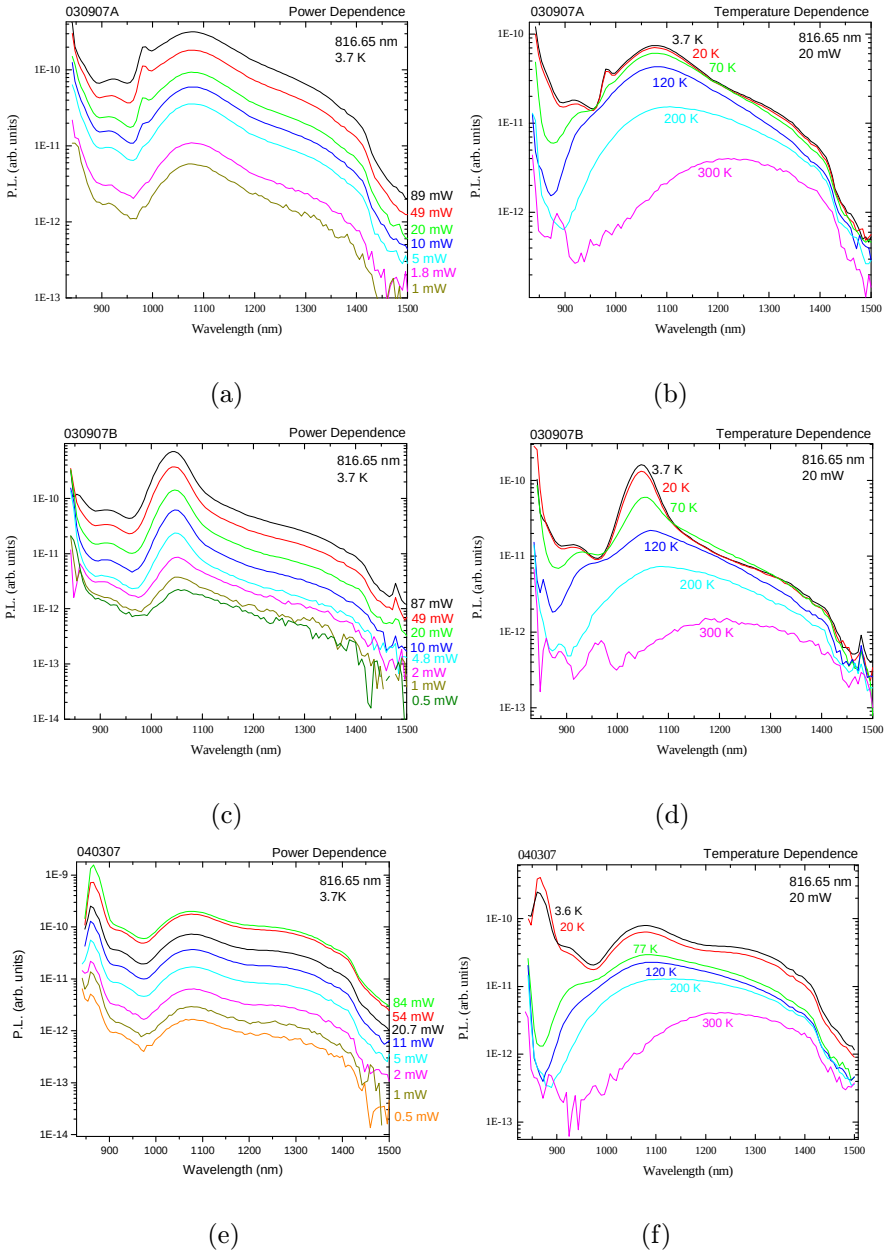

Figure 3.5 PL of samples 030907A, 030907B, and 040307. The peak below 1 μm, indicative of successful QD chain growth, is not present in these PL spectra.

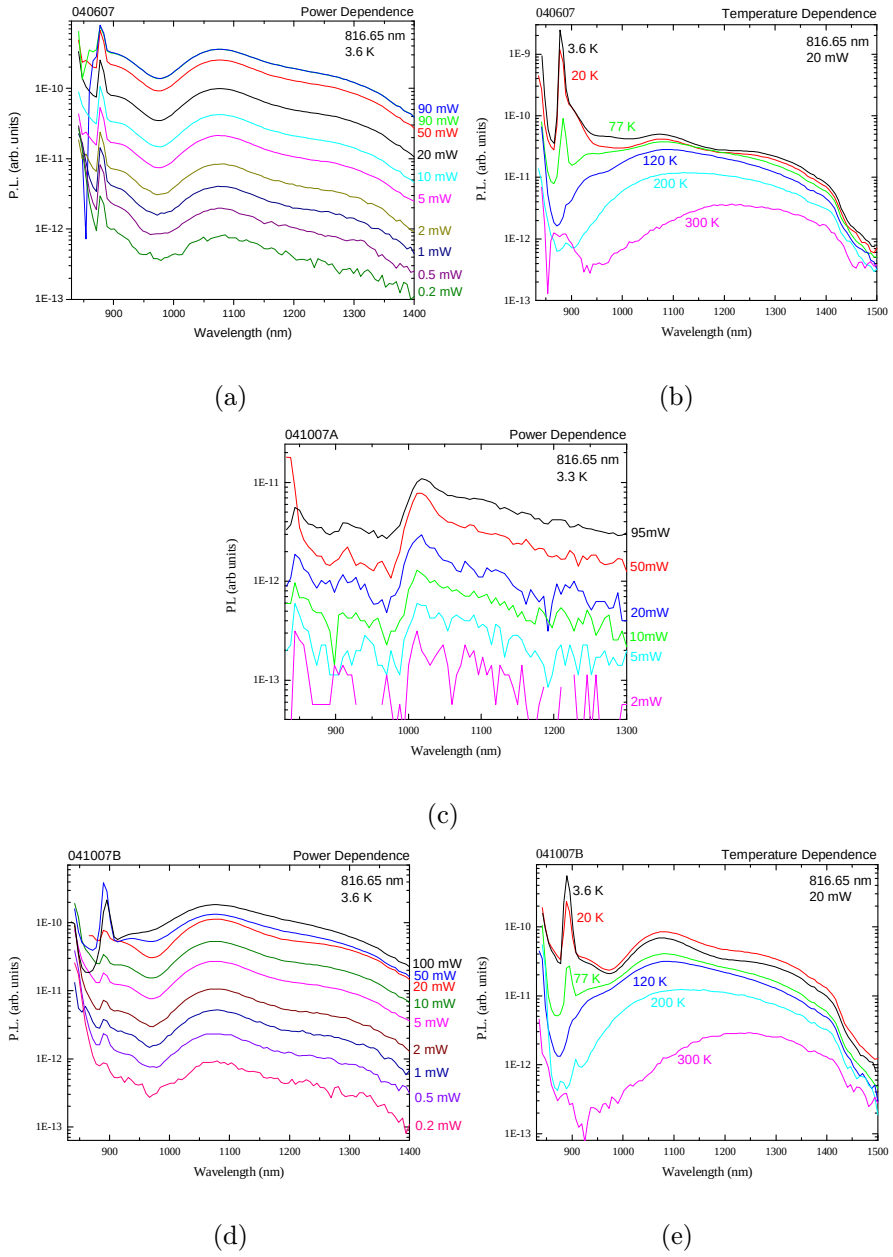

Figure 3.6 PL of samples 040607, 041007A, and 041007B. The peak below 1 μm, indicative of successful QD chain growth, is not present in these PL spectra.

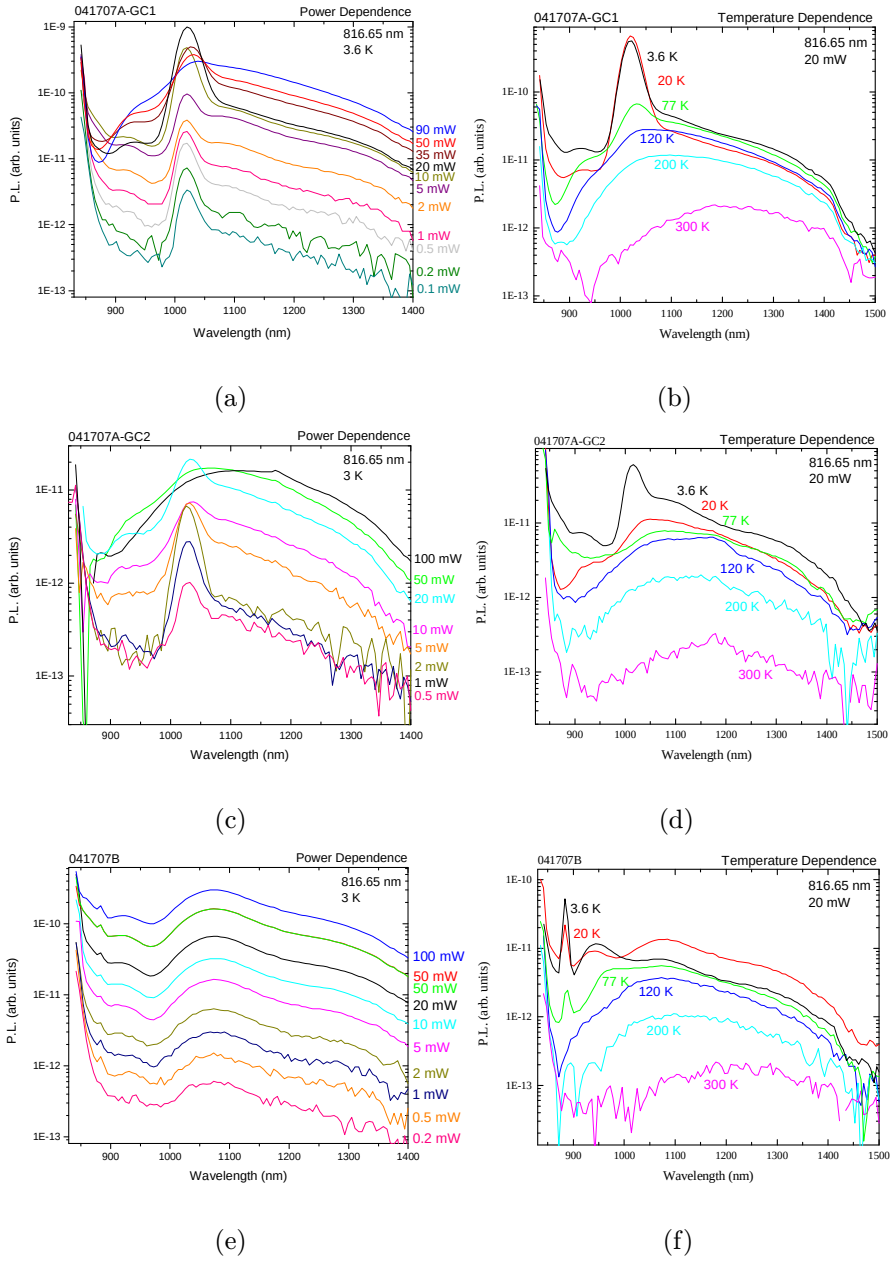

Figure 3.7 PL of samples 041707A-GC1, 041707A-GC2, and 041707B. The peak below 1 μm, indicative of successful QD chain growth, is not present in these PL spectra.

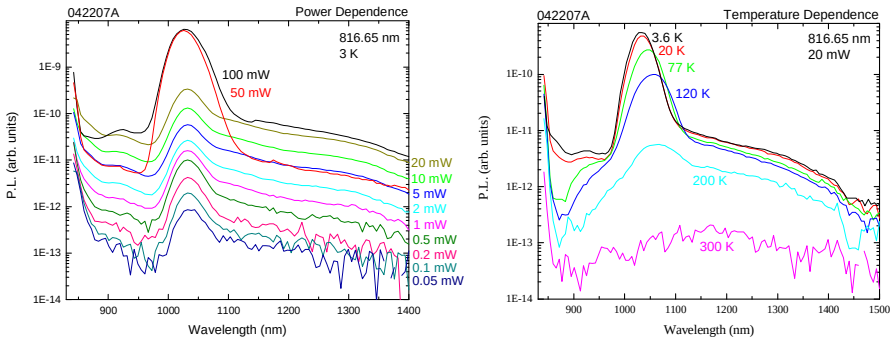

(a) (b)

Figure 3.8 PL of sample 042207A. The peak below 1 μm, indicative of successful QD chain growth, is not present in these PL spectra.

Chapter 4

Conclusion

Quantum dot samples grown using Dr. Haeyeon Yang's new growth method have been characterized through PL experiments. The presence of a sharp PL peak just below 1 μm indicates the successful creation of QD chains using Yang's growth method. However, these samples did not exhibit the state-filling effect commonly observed in similar samples, perhaps due to low power densities. Continued studies will more definitively determine whether Yang's method has produced QD chains in this sample set or not.

Appendix A

Table of Growth Parameters

Below is a table of the growth parameters for each sample received from Dr. Yang. After the growth of the WL, all samples were annealed for two minutes.

Table A.1 Growth parameters for each sample from Dr. Haeyeon Yang.

Sample	Buffer Growth	% As Growth	Growth Temp (°C)	Thickness of WL (ML)	Growth Time (s)	Chevrons Visible	Annealing Temp (°C)
022807	-	40	400	-	70	yes	480
032907	2h27m	25	390	10	47	no	520
040307	-	25	390	10	47	yes	550
030607A	2h3m	100	400	15	70	yes	520
030607B	2h10m	12	400	15	70	yes	520
030907A	1h40m	15	400	10	47	no	500
030907B	3h25m	20	400	10	47	yes	520
032607A	2h20m	25	395	10	47	no	500
032607B	1h52m	40	395	-	47	yes	540
040607A	1h44m	20	390	7.6	47	yes	510
041007A	1h23m	20	390	10.4?	50	yes	490
041007B	1h56m	20	390	-	50	yes	470
041707A	1h36m	20	390	10	50	no	450
041707B	-	20	390	-	50	yes	470
042207A	∼2h	20	390	-	50	-	490

Appendix B

Grating/Detector Response Correction

To account for the wavelength-dependent response of the monochromator gratings, the PL data should be divided by the appropriate grating response curve. All PL data in this thesis was obtained using the 500 nm grating. The response curves were obtained from the user's manuals.

B.1 DK 240 Monochromator Gratings

The response curves for the DK 240 Monochromator gratings are shown in Fig. B.1.

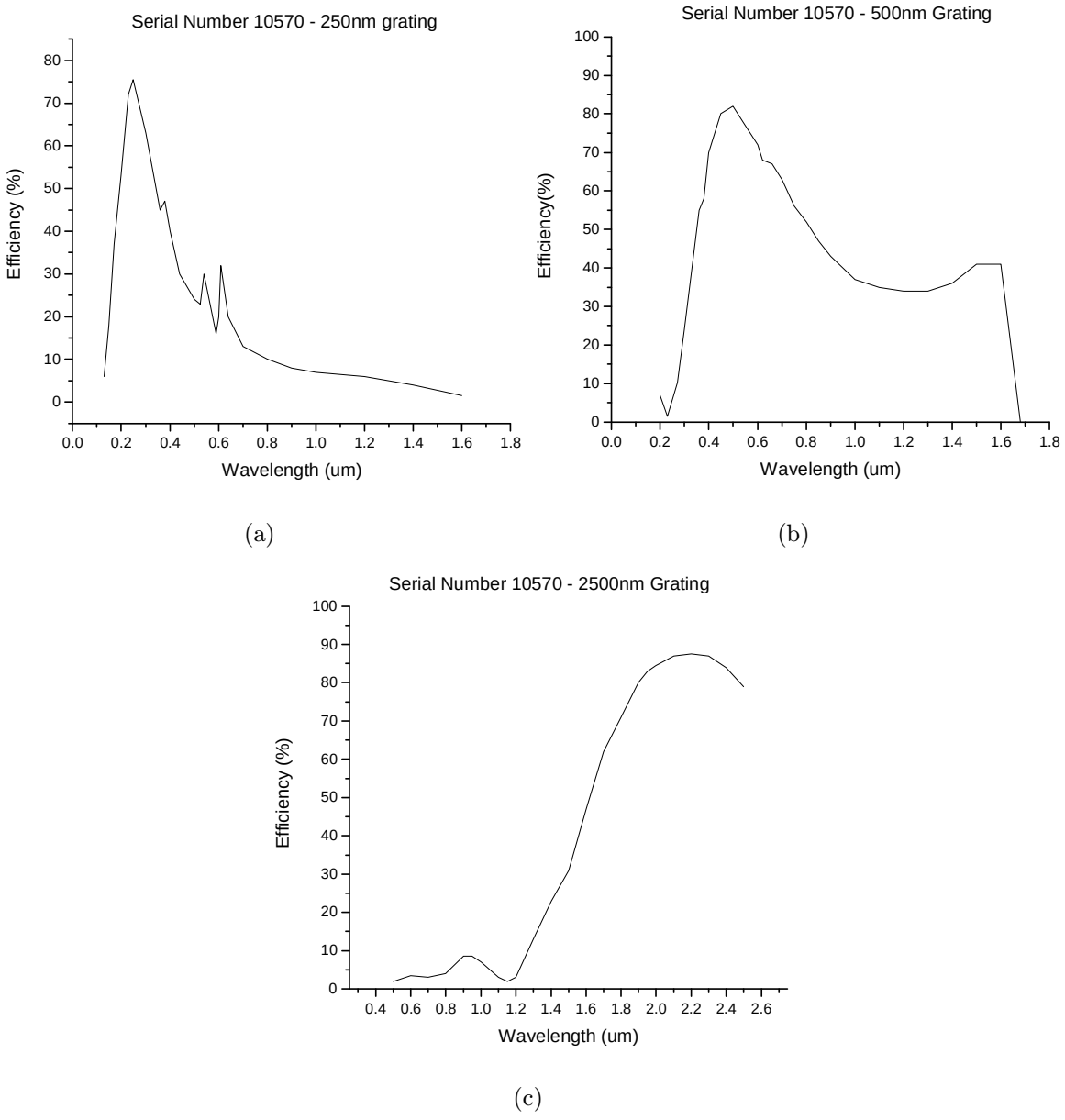

(a) (b)

(c)

Figure B.1 Grating response curves for the DK 240 Monochromator.

Appendix C

Reciprocal Linear Dispersion Calculation

After performing the experiments, I discovered that our monochromator has a wavelength-dependent reciprocal linear dispersion (RLD). This means that for a fixed slit width, the range of wavelengths that was exiting the monochromator and going into the detector was changing with the wavelength. This leads to a change in light intensity at the detector since the spread of wavelengths exiting the monochromator increases or decreases. This changing intensity then affects the overall PL curve. This is a documented problem, although it is often ignored by monochromator manufacturers [22]. Since our scans covered a wide range of wavelengths, the effects of non-constant RLD are significant, causing the range of wavelengths exiting the monochromator to change by 25% from 800 nm to 1500 nm. After researching more on this topic, I found a paper that addresses this problem - "Calculation of Dispersion for a Plane Grating in a Czerny-Turner Mount: a comment" [23]. The basic outline of a Czerny-Turner monochromator is given in Fig. C.1. Since the relation between the RLD and the angle r between the grating normal and the beam path cannot be

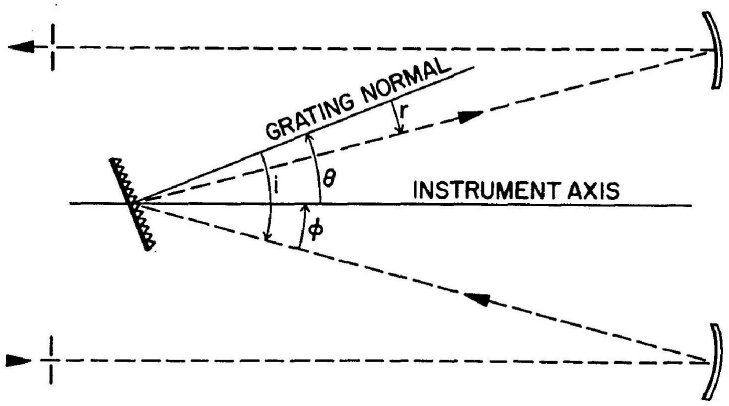

Figure C.1 The layout of a Czerny-Turner monochromator. The diagram originates from the paper of L. J. Radziemski regarding changing dispersion.

analytically solved, I had to write a Mathematica code that numerically solved this problem. The annotated code is given below.

Calculation of the change in dispersion versus wavelength of the CVI Digikrom 240, using equations and diagrams from references [22] and [23]:

"Calculation of the change in dispersion versus wavelength of the CVI Digikrom 240, using equations and diagrams from the following: http://www.opticsinfobase.org/DirectPDFAccess/C1F854BC-BDB9-137E- C2974E67707733 23_24929.pdf?da=1&id= 24929&seq=0&CFID =50627539&CFTOKEN=79126028";

$d = 1/1200 * 10\text{^}6//N; n = 1; f = 240;$

"d is groove spacing, 1/(1200 grooves/mm); n = order, f = focal length=240mm";

"This is the Reciprocal Linear Dispersion as a function of d, f, n and r";

dλoverdx=d*Cos[r*Pi/180]/(n*f)

$3.47222 Cos\left[\frac{\pi r}{180}\right]$

"I assume a constant relationship between i and r here";

$i = r + 2\phi; \phi = 9.45;$ "$\phi \sim$ ArcTan[M/L] = 18.9 degrees (assuming it's constant and measuring the monochromator to get M and L)";

$\lambda = d(\text{Sin}[i * \text{Pi}/180] + \text{Sin}[r * \text{Pi}/180])/n$

$833.333\left(Sin\left[\frac{\pi r}{180}\right] + Sin\left[\frac{1}{180}\pi(18.9 + r)\right]\right)$

$i = r + 2\phi; \phi = 9.45; d = 1/1200 * 10\text{^}6//N; n = 1; f = 240;$

$\lambda = d(\text{Sin}[i * \text{Pi}/180] + \text{Sin}[r * \text{Pi}/180])/n$

$833.333\left(Sin\left[\frac{\pi r}{180}\right] + Sin\left[\frac{1}{180}\pi(18.9 + r)\right]\right)$

$\lambda/.r \to (20.8)$

828.229

"Showing the starting and ending angle r for our scans from 830nm - 1500 nm";

$r/.\text{Solve}[833.33333(\text{Sin}[r * \text{Pi}/180] + \text{Sin}[18.92 * \text{Pi}/180 + r * \text{Pi}/180]) - 830 == 0, r][[1]]$

$r/.\text{Solve}[833.33333(\text{Sin}[r * \text{Pi}/180] + \text{Sin}[18.92 * \text{Pi}/180 + r * \text{Pi}/180]) - 1500 == 0, r][[1]]$

20.8624

56.3803

"Graph showing the Wavelength out of the monochromator as a function of the angle r";

$\lambda 1$=d(Sin[i*Pi/180]+Sin[r*Pi/180])/n

j = Table[{$r, \lambda 1$}, {$r, 0, 70, .1$}];

ListPlot[j, PlotRange → {{0, 70}, {200, 1700}}, AxesLabel → {Angle r (degrees), Wavelength Out (nm)}]

$$833.333\,(Sin\,[\tfrac{\pi r}{180}] + Sin\,[\tfrac{1}{180}\pi(18.9 + r)])$$

dλoverdx = $d * \text{Cos}[r * \text{Pi}/180]/(n * f)$;

k = Table[{r, dλoverdx}, {$r, 0, 70, .1$}];

j2 = Flatten[Table[{$\lambda 1$}, {$r, 0, 60, .1$}]];

k2 = Flatten[Table[{dλoverdx}, {$r, 0, 60, .1$}]];

Both = Riffle[j2, k2];

Final = Partition[Both, 2];

Final graph showing the change in dispersion versus wavelength;

Dataplot = ListPlot[Final, PlotRange → {{600, 1700}, {0, 3.5}}, AxesLabel → {Wavelength (nm), $\frac{\text{D}\lambda}{\text{DX}}$ ($\frac{\text{NM}}{\text{MM}}$)}]

Guess = Plot[3.4Cos[$(x - 600)/1000$], {x, 600, 1700}, AxesOrigin → {600, 0}]

Show[%%, %]

fitty = Fit[Final, {$1, x, x\text{^}2, x\text{^}3, x\text{^}4$}, x]

Fitty[x_] = fitty; Fitty[x_]

QuarticPlot = Plot[fitty, {x, 600, 1700}, PlotRange → {{600, 1700}, {0, 3.5}}];

Show[QuarticPlot, Dataplot]

Length[Final]

601

Q = Table[{Final[[i]][[1]], Final[[i]][[2]]/Fitty[Final[[i]][[1]]]}, {i, 1, 601}];

ListPlot[%, PlotRange → {{830, 1500}, {.99, 1.01}}, AxesLabel → {Wavelength (nm), $\frac{\text{D}\lambda}{\text{DX}}$ ($\frac{\text{NM}}{\text{MM}}$)}, AxesOrigin → {830, .99}]

Solve[Fitty[x] == 3, x]

$$\{\{x \to -100.057\}, \{x \to 916.802 - 1048.46i\}, \{x \to 916.802 + 1048.46i\}, \{x \to 1052.34\}\}$$

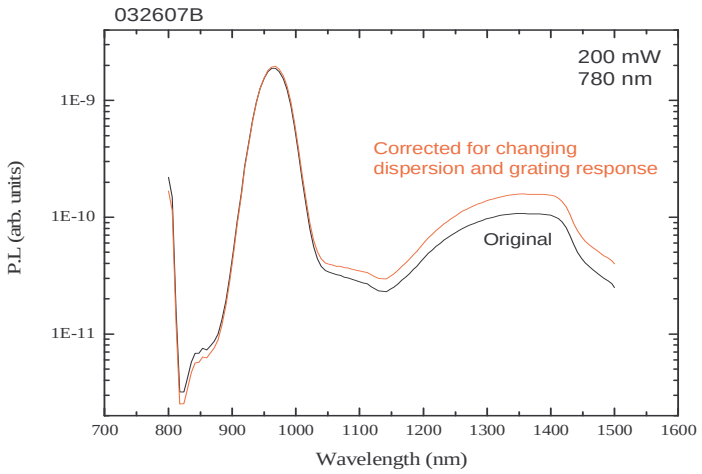

Figure C.2 Data corrected for the changing reciprocal dispersion and the grating efficiency. The correction did not significantly alter the overall shape of the data.

Bibliography

[1] H. C. Liu, M. Gao, J. McCaffrey, Z. R. Wasilewski, and S. Fafarda, "Quantum Dot Infrared Photodetectors," Appl. Phys. Lett. **78,** 79–81 (2001).

[2] V. A. Egorov, G. E. Cirlin, N. K. Polyakov, V. N. Petrov, A. A. Tonkikh, B. V. Volovik, Y. G. Musikhin, A. E. Zhukov, A. F. Tsatsulnikov, and V. M. Ustinov, "1.3-1.4 μm Photoluminescence Emission from InAs/GaAs Quantum Dot Multilayer Structures Grown on GaAs Singular and Vicinal Substrates," Nanotech. **11,** 323–326 (2000).

[3] Z. M. Wang, K. Holmes, Y. I. Mazur, and G. J. Salamo, "Fabrication of (In,Ga)As quantum-dot chains on GaAs(100)," Appl. Phys. Lett. **84,** 1931–1933 (2004).

[4] J. H. Lee, Z. M. Wang, B. L. Liang, W. T. Black, V. P. Kunets, Y. I. Mazur, and G. J. Salamo, "Selective Growth of InGaAs/GaAs Quantum Dot Chains on Pre-Patterned GaAs(100)," Nanotechnology **17,** 2275–2278 (2006).

[5] D. J. Kim and H. Yang, "Shape Control of InGaAs Nanostructures on Nominal GaAs(001): Dashes and Dots," Nanotechnology **19,** 1–5 (2008).

[6] D. Gammon, E. S. Snow, B. V. Shanabrook, D. S. Katzer, and D. Park, "Fine Structure Splitting in the Optical Spectra of Single GaAs Quantum Dots," Phys. Rev. Lett. (1996).

[7] G. Schmid, *Nanoparticles: From Theory To Application* (Wiley-VCH, Germany, 2004), Vol. 1, pp. 25–27.

[8] M. Skolnick and D. Mowbray, "Self-Assembled Semiconductor Quantum Dots: Fundamental Physics and Device Applications," Annu. Rev. Mater. Res. **34,** 181–218 (2004).

[9] Z. M. Wang, *Self-Assembled Quantum Dots* (Springer Science+Business Media, LLC, New York, 2008).

[10] A. L. Rogach, *Semiconductor Nanocrystal Quantum Dots Synthesis, Assembly, Spectroscopy and Applications* (Springer Science+Business Media, LLC, New York, 2008), Vol. 1, specifically see pages 3-5 for a more complete description of nanocrystal synthesis techniques.

[11] S. Bose, "Quantum Communication through an Unmodulated Spin Chain," Phys. Rev. Lett. **91,** 1–4 (2003).

[12] G. Y. Slepyan, Y. D. Yerchak, A. Hoffmann, and F. G. Bass, "Strong Electron-Photon Coupling in One-Dimensional Quantum Dot Chain: Rabi Waves and Rabi Wavepackets," http://www.citebase.org/abstract?id=oai:arXiv.org:0907.3191 (2009).

[13] J. Tatebayashi, M. Nishioka, and Y. Arakawa, "Over 1.5 μm light emission from InAs quantum dots embedded in InGaAs strain-reducing layer grown by metalorganic chemical vapor deposition," Appl. Phys. Lett. **78,** 3469–3471 (2001).

[14] D. Bimberg, M. Grundmann, and N. N. Ledentsov, *Quantum dot heterostructures* (Wiley-VCH, New York, 2001), pp. 145–146.

[15] W. Seifert, N. Carlsson, M. Miller, M.-E. Pistol, L. Samuelson, and L. R. Wallenberg, "In-Situ Growth Of Quantum Dot Structures By The Stranski-Krastanow Growth Mode," Progress in Crystal Growth and Characterization of Materials **33,** 423–471 (1996).

[16] H. Yang, D. Kim, A. M. Jones, J. S. Colton, D. Smith, S. Thalman, and S. Brown, "Optical Properties of InGaAs Quantum Dots and Chains Induced by Annealing on GaAs(001)," (in preparation).

[17] H. Yang, "Suppression of Segregation and Intermixing for Novel Nanostructures," colloquium, Department of Physics, Brigham Young University, (Provo, Utah, February 11, 2009).

[18] X. Y. Wang, Y. I. Mazur, W. Q. Ma, Z. M. Wang, G. J. Sdamo, M. Xiao, T. Mishima, and M. Johnson, "Transition from a Quantum-Dot to a Quantum-Wire Electronic Structure in InGaAs/GaAs Quantum-Dot Chains," IEEE p. http://ieeexplore.ieee.org/stamp/stamp.jsp?arnumber=01276280 (2003?).

[19] W.-H. Chang, T.-M. Hsu, Kuei-FenTsai, T.-E. Nee, J.-I. Chyi, and N.-T. Yeh, "Excitation Density and Temperature Dependent Photoluminescence of InGaAs Self-Assembled Quantum Dots," Jpn. J. Appl. Phys. **38,** 554–557 (1999).

[20] X. Y. Wang, W. Q. Ma, J. Y. Zhang, G. J. Salamo, M. Xiao, and C. K. Shih, "Photoluminescence Intermittency of InGaAs/GaAs Quantum Dots Confined in a Planar Microcavity," Nano Lett. **5,** 1873–1877 (2005).

[21] V. Türck, F. Heinrichsdorff, M. Veit, R. Heitz, M. Grundmann, A. Krost, and D. Bimberg, "Correlation of InGaAs/GaAs Quantum Dot and Wetting Layer Formation," Applied Surface Science **123,** 352–355 (1998).

[22] F. Maessen and J. Tielrooij, "Dispersion of Grating Monochromators," Fresenius' Journal of Analytical Chemistry **323,** 460 (1986).

[23] L. Radziemski, "Calculation of Dispersion for a Plane Grating in a Czerny-Turner Mount: a comment," App. Optics **20,** 1948–1950 (1981).